

General gravitational properties of neutron stars: curvature invariants, binding energy, and trace anomaly

Iván Garibay,^{1,2} Christian Ecker,¹ and Luciano Rezzolla^{1,3,4}

¹*Institut für Theoretische Physik, Goethe Universität, Max-von-Laue-Str. 1, 60438 Frankfurt am Main, Germany*

²*Instituto de Astronomía, Universidad Nacional Autónoma de México, Ciudad de México, CDMX 04510, Mexico*

³*School of Mathematics, Trinity College, Dublin 2, Ireland*

⁴*Frankfurt Institute for Advanced Studies, Ruth-Moufang-Str. 1, 60438 Frankfurt am Main, Germany*

(Dated: January 14, 2026)

We investigate the behavior of curvature invariants for a large ensemble of neutron stars built with equations of state (EOSs) that satisfy constraints from nuclear theory and perturbative QCD, as well as measurements of neutron-star masses, radii, and gravitational waves from binary neutron-star mergers. Surprisingly, our analysis reveals that stars with negative Ricci scalar \mathcal{R} are rather common and about $\sim 50\%$ of our EOSs produce one or more stars with Ricci curvature that is negative somewhere inside the star. The negative curvature is found mostly but not exclusively at the highest densities and pressures, and predominantly for stiff EOSs and for the most compact and most massive stars. Furthermore, we improve the quasi-universal relation between the stellar gravitational mass M and the baryonic mass M_b , which allows us to express analytically one in terms of the other with a maximum variance of only $\sim 3\%$. Finally, using the relation between the Ricci scalar and the trace anomaly Δ , we determine the conditions under which Δ vanishes or becomes negative in neutron stars.

Keywords: neutron stars – equation of state – trace anomaly – curvature scalars

I. INTRODUCTION

The extreme conditions inside neutron stars (NSs) present a major challenge for the theoretical modelling of nuclear matter at densities several times higher than the saturation density of atomic nuclei, $n_s := 0.16 \text{ fm}^{-3}$. While effective field theory remains one of the most powerful tools for predicting the behaviour of dense matter, its uncertainties grow significantly at the high densities characteristic of NS cores. On the other hand, first-principles perturbative Quantum Chromodynamics (QCD) calculations are reliable only at densities far exceeding those found in NSs, but they still offer valuable consistency checks for modelling matter at lower densities [1–11]. As a result, our theoretical understanding of fundamental properties – such as the equation of state (EOS) of dense nuclear and quark matter – remains limited. To counter this and make progress on our understanding of NSs, agnostic or phenomenological approaches are employed to construct the EOS at NS densities. At the same time, recent and forthcoming observations of NSs and their mergers offer a unique opportunity to probe strongly coupled dense matter under conditions that are otherwise inaccessible in terrestrial experiments.

It is therefore essential to integrate existing theoretical insights with observational data to constrain the EOS and related quantities that govern the macroscopic properties of NSs. Thus far, the primary focus of this effort has been on the EOS itself, with significant progress achieved through the use of generic parametrizations combined with statistical methods to derive robust constraints on the distribution of masses and radii from theoretical and astrophysical inputs [12]. This has been followed by more targeted studies aimed at constraining quantities closely tied to the EOS, such as the speed of sound [13–18] and the trace (conformal) anomaly [19–24].

However, in addition to these physically measurable quantities, the use of parameterized EOSs also allows one to explore more geometrical properties of NSs that, while not measurable,

provide important insights in the gravitational properties of these objects and, ultimately, about gravity under extreme conditions. Given the general information about curvature that is accessible via the Riemann tensor, the curvature scalars that can be constructed from it and its variants, such as the Ricci scalar \mathcal{R} and the Kretschmann scalar \mathcal{K}_1 , provide quantitative information about the internal geometry of NSs.

In this context, interesting studies on curvature scalars and their role in alternative theories of gravity, dark-matter components, and anisotropic EOSs have already been presented in the literature [see, e.g., 25–30]. All of these studies, however, have concentrated on specific EOSs and have not really explored the behaviour of curvature-related quantities in NSs within an agnostic description of the EOSs. As a result, the existence of quasi-universal behaviour of geometry and gravitationally related quantities has not been explored yet and represents the main goal of this work. More specifically, we here present a systematic investigation of the behaviour within the star of various curvature invariants and highlight the conditions under which they can become negative. Furthermore, we statistically improve previous studies on the quasi-universal relation between the baryonic and gravitational mass, compactness and binding energy of NSs. Finally, we relate the properties of the Ricci scalar with those of the trace anomaly and illustrate the non-trivial correlation that exists between the two as a function of the stellar mass.

The plan of the paper is as follows. In Sec. II we briefly describe the numerical implementation of our set of constrained parametric EOSs. Additionally, we include the mathematical formalism for the curvature scalars and their relation with the matter content inside NSs. In Sec. III we present and discuss our results, while Sec. IV is dedicated to our conclusions and prospects for future research. Geometric units in which $c = G = 1$ are used throughout this work and we adopt the standard notation for the summation on repeated tensor indices, which we take to run from 0 to 3 and indicate with

Greek letters.

II. METHODS

A. Stellar Equilibrium Models

To construct static and spherically symmetric stellar models in hydrostatic equilibrium we assume the matter to be described by a perfect fluid with energy-momentum tensor [31]

$$T^{\mu\nu} = (e + p) u^\mu u^\nu + p g^{\mu\nu}, \quad (1)$$

where u^μ are the components of the fluid four-velocity, $g^{\mu\nu}$ is the metric tensor, and p and e are the pressure and energy density, respectively.

Einstein's equations, together with the conservation of the energy-momentum tensor, reduce to the relativistic hydrostatic equilibrium equation

$$\frac{dp}{dr} = -\frac{me}{r^2} \left(1 + \frac{p}{e}\right) \left(1 + \frac{4\pi r^3 p}{m}\right) \left(1 - \frac{2m}{r}\right)^{-1}, \quad (2)$$

where r is the radial coordinate, while the integrated mass $m = m(r)$ enclosed within r follows the differential equation

$$\frac{dm}{dr} = 4\pi r^2 e. \quad (3)$$

Equations (2)–(3) are also known as the Tolman-Oppenheimer-Volkov (TOV) equations.

Given an EOS, $p = p(e)$, a unique star with stellar radius R and stellar mass M is defined imposing the set of boundary conditions at the centre of the star, $e(0) = e_c$ and $m(0) = 0$; and at the surface of the star $r = R$, where $p(R) = 0$ and $M := m(R)$. The maximum stable mass achieved by an EOS will be denoted hereafter by M_{TOV} .

B. Equations of State

Our construction of the EOSs follows closely the framework of Altiparmak *et al.* [18], and we thus generate a large ensemble by combining established models in different density regimes: the Baym-Pethick-Sutherland (BPS) model [32] for the crust, polytropic segments sampled between soft and stiff nuclear-theory bounds [33] up to $1.1 n_s$, and perturbative QCD results [1] at baryon chemical potentials above 2.6 GeV. In the intermediate density regime relevant for NSs, we adopt the piecewise-linear sound-speed parametrization introduced by Annala *et al.* [3], where $c_s^2 := \partial p / \partial e$ is the speed of sound. This approach allows one to obtain a smooth interpolation between nuclear and quark matter. For our Bayesian inference we use a uniform prior distribution of our parameters – the piecewise speeds of sound with $N = 7$ segments – within the allowed interval, $c_{s,i}^2 \in [0, 1]$.

To constrain this set, we retain only EOSs compatible with astrophysical observations. These include: the existence of $\sim 2 M_\odot$ NSs [34–36], NICER radius measurements of

pulsars J0740+6620 and J0030+0451 [37–40], and the tidal deformability constraint from the gravitational waves event GW170817 [41]. Specifically, we impose the following cut-off filters through our likelihood function: $M_{\text{TOV}} > 2.08 M_\odot$; radii $R > 10.75$ km for $2.0 M_\odot$ NSs; $R > 10.8$ km for $1.1 M_\odot$ NSs; and a tidal deformability $\tilde{\Lambda} < 720$ for a binary of NSs with chirp mass $\mathcal{M}_{\text{chirp}} = 1.186 M_\odot$ and mass ratio $q > 0.73$. Varying the values of our parameters with a Goodman and Weare's Affine invariant Markov chain Monte Carlo ensemble sampler [42]¹, we obtain a posterior of approximately 3×10^4 viable EOSs.

C. Curvature Invariants

We recall that in general relativity, the curvature of spacetime is encoded in the Riemann tensor. A natural approach to investigate the connection between the properties of the EOS and the spacetime curvature in NSs consists of considering coordinate (gauge)-independent measures of curvature, namely scalar curvature invariants, which are constructed by contracting tensor products of the Riemann tensor with itself and other geometric objects. While there are 14 independent second-order curvature scalar invariants [43], in this work we focus on the Ricci scalar, together with the three independent quadratic curvature invariants formed from contractions of the Riemann tensor and the Levi-Civita tensor. Our discussion here closely follows [44], where the same scalars are analyzed in the context of binary NS mergers for a small set of EOSs with phase transitions [45].

More specifically, using the Ricci tensor, $\mathcal{R}_{\mu\nu}$, it is possible to compute its full contraction

$$\mathcal{J}^2 := \mathcal{R}_{\mu\nu} \mathcal{R}^{\mu\nu}. \quad (4)$$

as well as its contraction with the metric tensor $g^{\mu\nu}$, which yields the well-known Ricci scalar

$$\mathcal{R} := \mathcal{R}_{\mu\nu} g^{\mu\nu} = \mathcal{R}^\mu_\mu, \quad (5)$$

which plays a fundamental role in Einstein equations.

Other quadratic invariants – known as the Kretschmann scalar \mathcal{K}_1 , the Chern-Pontryagin scalar \mathcal{K}_2 , and the Euler scalar \mathcal{K}_3 – constitute the principal invariants of the Riemann tensor on four-dimensional Lorentzian manifolds [46], and are defined as follows:

$$\mathcal{K}_1 := \mathcal{R}_{\mu\nu\rho\sigma} \mathcal{R}^{\mu\nu\rho\sigma}, \quad (6)$$

$$\mathcal{K}_2 := {}^* \mathcal{R}_{\mu\nu\rho\sigma} \mathcal{R}^{\mu\nu\rho\sigma}, \quad (7)$$

$$\mathcal{K}_3 := {}^* \mathcal{R} {}^*_{\mu\nu\rho\sigma} \mathcal{R}^{\mu\nu\rho\sigma}, \quad (8)$$

where the left and right duals of a generic four-index tensor $\mathcal{A}_{\mu\nu\rho\sigma}$ are defined via contractions with the Levi-Civita tensor $\epsilon_{\mu\nu\alpha\beta}$:

$${}^* \mathcal{A}_{\mu\nu\rho\sigma} := \epsilon_{\mu\nu\alpha\beta} \mathcal{A}^{\alpha\beta}_{\rho\sigma}, \quad (9)$$

$$\mathcal{A}^*_{\mu\nu\rho\sigma} := \mathcal{A}_{\mu\nu}^{\alpha\beta} \epsilon_{\alpha\beta\rho\sigma}. \quad (10)$$

¹ From the Python package emcee.

Note that \mathcal{K}_2 can equivalently be defined using the right dual instead of the left dual; the difference is irrelevant for our purposes.

Using the Weyl tensor, that is, the trace-free part of the Riemann tensor

$$\mathcal{W}_{\mu\nu\rho\sigma} := \mathcal{R}_{\mu\nu\rho\sigma} - (g_{\mu[\rho}\mathcal{R}_{\sigma]\nu} - g_{\nu[\rho}\mathcal{R}_{\sigma]\mu}) + \frac{1}{3}\mathcal{R}g_{\mu[\rho}g_{\sigma]\nu}, \quad (11)$$

where the square brackets denote antisymmetric tensor indices, it is possible to compute two additional invariants defined as

$$\mathcal{I}_1 := \mathcal{W}_{\mu\nu\rho\sigma}\mathcal{W}^{\mu\nu\rho\sigma}, \quad (12)$$

$$\mathcal{I}_2 := {}^*\mathcal{W}_{\mu\nu\rho\sigma}\mathcal{W}^{\mu\nu\rho\sigma}. \quad (13)$$

These are the only linearly independent principal invariants of the four-dimensional Weyl tensor, since

$${}^*\mathcal{W}^*_{\mu\nu\rho\sigma}\mathcal{W}^{\mu\nu\rho\sigma} = -\mathcal{I}_1. \quad (14)$$

The invariants introduced so far are not linearly independent and are indeed related via the following equations [46]

$$\mathcal{K}_1 = \mathcal{I}_1 + 2\mathcal{J}^2 - \frac{1}{3}\mathcal{R}^2, \quad (15)$$

$$\mathcal{K}_2 = \mathcal{I}_2, \quad (16)$$

$$\mathcal{K}_3 = -\mathcal{I}_1 + 2\mathcal{J}^2 - \frac{2}{3}\mathcal{R}^2. \quad (17)$$

Furthermore, since we are considering static, spherically symmetric, and asymptotically flat spacetimes, \mathcal{K}_2 – and hence \mathcal{I}_2 – are identically zero [47].

D. Energy-Momentum Tensor and Trace-Anomaly

Given the energy-momentum tensor of a perfect fluid (1) and a timelike 4-velocity u^μ with unit norm $u^\mu u_\mu = -1$, the trace of the energy-momentum tensor is simply given by

$$T := T^{\mu\nu}g_{\mu\nu} = 3p - e. \quad (18)$$

We can now use Eq. (18) to introduce a basic diagnostic of the EOS behavior, namely, the so-called trace (or “conformal”) anomaly², which is defined as

$$\Delta := \frac{1}{3} - \frac{p}{e} = -\frac{T}{3e}. \quad (19)$$

Note that since $e \geq 0$, then $T \leq 0$ ($T > 0$) when $\Delta \geq 0$ ($\Delta < 0$).

This dimensionless quantity measures deviations from conformal symmetry and is bounded by causality and thermodynamic stability within $-2/3 \leq \Delta \leq 1/3$. It is worth mentioning that the sector $\Delta < 0$ does not imply violation of causality, since

² The “conformal” nomenclature comes from the fact that for a conformal fluid $p = e/3$, so that $\Delta \neq 0$ measures the anomaly with respect to a conformal fluid.

theoretical relativistic EOSs can be constructed with $\Delta < 0$, as noted by Zel'dovich [48]. Obviously, causality also requires a subluminal speed of sound of the EOS, *i.e.*, $0 \leq c_s \leq 1$. In the context of model-agnostic parametrizations of NS matter, a conformal anomaly approaching zero has been used as an indicator of a deconfinement transition to quark matter [22, 49], a trend that has been confirmed by microphysical modeling of deconfinement [24].

For a static and spherically symmetric perfect fluid, it is possible to write explicit relations between the trace anomaly and some of the curvature scalars, *i.e.*, \mathcal{R} , \mathcal{J}^2 , and \mathcal{I}_1 . More specifically, we introduce the following normalised quantities

$$\bar{e} := \frac{3m}{4\pi r^3}, \quad (20)$$

$$\Psi := 1 - \frac{\bar{e}}{e}, \quad (21)$$

where \bar{e} is the mean density enclosed within a sphere of coordinate radius r and Ψ measures the deviation of the energy density e from \bar{e} . In this way, the following expressions can be obtained

$$\mathcal{R} = 24\pi e\Delta, \quad (22)$$

$$\mathcal{J}^2 = 64\pi^2 e^2 \left[1 + 3 \left(\frac{1}{3} - \Delta \right)^2 \right], \quad (23)$$

$$\mathcal{I}_1 = \frac{256}{3}\pi^2 e^2 \Psi^2 = \frac{256}{3}\pi^2 \left(\frac{3m}{4\pi r^3} - e \right)^2, \quad (24)$$

Since the solution of the TOV equations (2)–(3) amounts to computing the (radial) functional behaviour of $e = e(r)$, $p = p(r)$, and $m = m(r)$, we can use the relations (15)–(17), together with (22)–(24), to derive the radial profile of the curvature scalars $\mathcal{K}_1 = \mathcal{K}_1(r)$ and $\mathcal{K}_3 = \mathcal{K}_3(r)$ inside the NSs. Finally, another useful scalar quantity whose behaviour inside the star can be of interest is simply given by the local stellar compactness

$$\eta(r) := \frac{m(r)}{r}, \quad (25)$$

which increases from zero to its maximum value η_{\max} close to the crust [25]³. It should be noted that η_{\max} is in general larger than the asymptotic value of $\eta(r)$, *i.e.*, $\mathcal{C} := \lim_{r \rightarrow \infty} \eta(r) = M/R$, which is also referred to as the (asymptotic) stellar compactness. It has been recently argued that $\mathcal{C} \leq 1/3$ for realistic NSs [50] and indeed all of our stellar models are consistent with this upper bound.

III. RESULTS

A. Ricci Scalar

Figure 1 presents with a colormap the radial profiles of probability distribution functions (PDFs) for the Ricci scalar

³ We note that our definition of compactness differs by a factor of two from that given by [25].

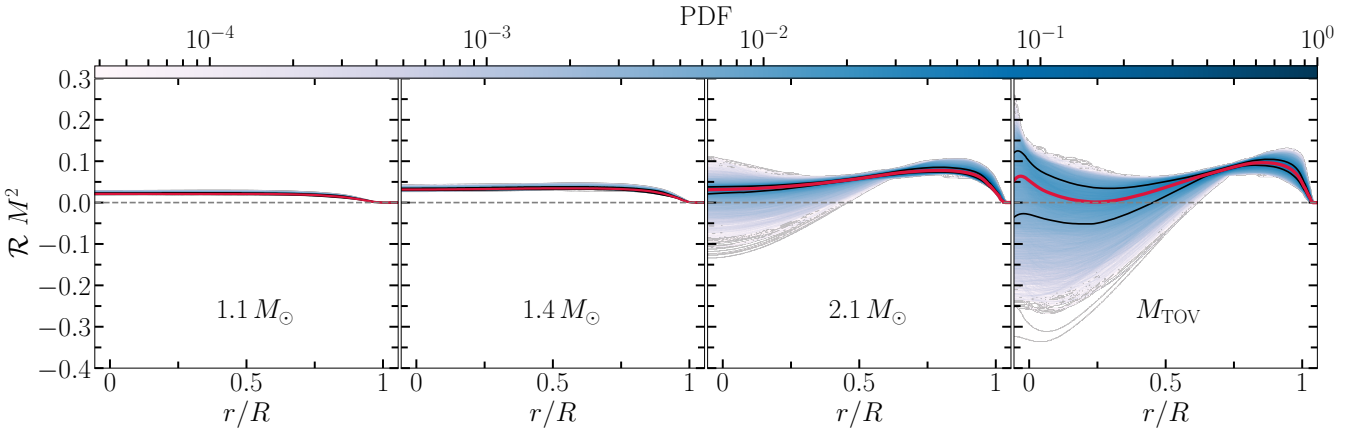


FIG. 1. Normalized PDFs of the radial profiles of the normalized Ricci scalar $\mathcal{R} M^2$ for fixed NS masses. The red lines mark the median values of the distribution, while black lines correspond to $1-\sigma$ confidence limits. From left to right: the profiles refer to NSs with masses $1.1 M_\odot$, $1.4 M_\odot$, $2.1 M_\odot$ and M_{TOV} , respectively.

relative to all of the stellar models considered and for every EOS. Since the distributions vary considerably with the mass, we report in the first panels from the left the radial profiles for a fixed mass of 1.1 , 1.4 , and $2.1 M_\odot$; the last and fourth panel, on the other hand, collects stellar models at the maximum mass M_{TOV} , which have larger variation since different EOSs will in general feature significantly different maximum masses. Note that the plots refer to dimensionless quantities since the Ricci scalar is scaled by the square of the NS mass, $\mathcal{R} M^2$, and the radial position is rescaled by the corresponding stellar radius, r/R . The red solid line represents the median-value of the distribution, while the black solid lines correspond to the $1-\sigma$ deviation from it.

When concentrating for simplicity on the median values, the first two panels from the left in Fig. 1 clearly show that the Ricci scalar is always positive and essentially constant across the star, retaining the value at the centre up to the outer layers of the star, where $\mathcal{R} \rightarrow 0$, as the stellar surface is approached. At the same time, when considering the mass-cut at $2.1 M_\odot$ (third panel), it is possible to note that the Ricci scalar is no longer monotonic and that it actually increases to a local maximum around $r/R \simeq 0.7$ to then decrease towards the surface. Also, while the average value is always positive, a small portion of the EOSs does show stellar models with negative Ricci scalar in the stellar core. This behaviour is magnified when considering a mass cut at $M = M_{\text{TOV}}$, as shown in the fourth (rightmost) panel of Fig. 1. In this case, in fact, it is possible to note that \mathcal{R} is not only non-monotonic, but that it can have negative values in the inner regions of the stars. Indeed, while the median value of $\mathcal{R} > 0$ for $r/R \simeq 0$, it vanishes for $r/R \simeq 0.25$. The Ricci scalar then grows to a local maximum near the stellar surface and naturally vanishes as the stellar surface is approached. We should note that for the static fluid configurations considered here, $\mathcal{R}_{\mu\nu} u^\mu u^\nu > 0$ everywhere, so that – using the Raychaudhuri equation – timelike geodesics would still be focussed even in regions where $\mathcal{R} < 0$ [31].

The left panel of Fig. 2 displays with two colormaps the

PDFs of the Ricci scalar as a function of the mass and radii of the various stellar models. More specifically, while the green colormap is used for those stellar models having non-negative Ricci scalar, i.e., $\mathcal{R} \geq 0$, everywhere inside the star, the red colormap corresponds to those NSs with negative Ricci scalar, i.e., $\mathcal{R} < 0$, somewhere inside the star. In both cases, $1-\sigma$, $2-\sigma$ confidence levels are shown with darker and lighter shades of the colours, while the solid grey line marks the 100%-confidence interval. The distributions clearly show that more compact stars are more likely to have negative values of the Ricci scalar and this can happen either at small radii ($R \simeq 11$ km) and with comparatively small masses ($M \gtrsim 2.0 M_\odot$) or at larger radii ($R \simeq 13$ km) and with comparatively large masses ($M \gtrsim 2.3 M_\odot$). Also worth remarking is that the most compact stars – and hence massive stars for those EOSs [see 50, for a conjecture relating the maximum compactness to the maximum mass] – all have a negative Ricci scalar somewhere in their interior.

Note also that the two regions with $\mathcal{R} \leq 0$ are not distinct but they overlap. This can be appreciated from the projections of the 100%-confidence intervals of the distribution as a function of the stellar radius (red and green solid lines on the top part of the panel) and of the stellar mass (red and green solid lines on the right part of the panel). The local maxima at $M \sim 2.3 M_\odot$ and $R \sim 12.5$ km simply reflect a higher concentration of stellar models in those regions [18].

From our collection of EOSs, about 51% of them leads to NSs with $\mathcal{R} > 0$ everywhere in their interior. While the rest of EOSs produce at least one NS with $\mathcal{R} < 0$ somewhere in their interior. We note that, for every EOS, it is possible to determine the “zero-curvature” compactness \mathcal{C}_0 , that is, the ratio M/R at which the stellar model has zero Ricci curvature at the centre, i.e., $\mathcal{R}(r=0) = 0$ ⁴. Interestingly, it was shown in [51] using

⁴ After fixing the EOS, it is possible that two NSs have $\mathcal{R}(r=0) = 0$ (see also the discussion on Fig. 6 below); when this happens, and in order to

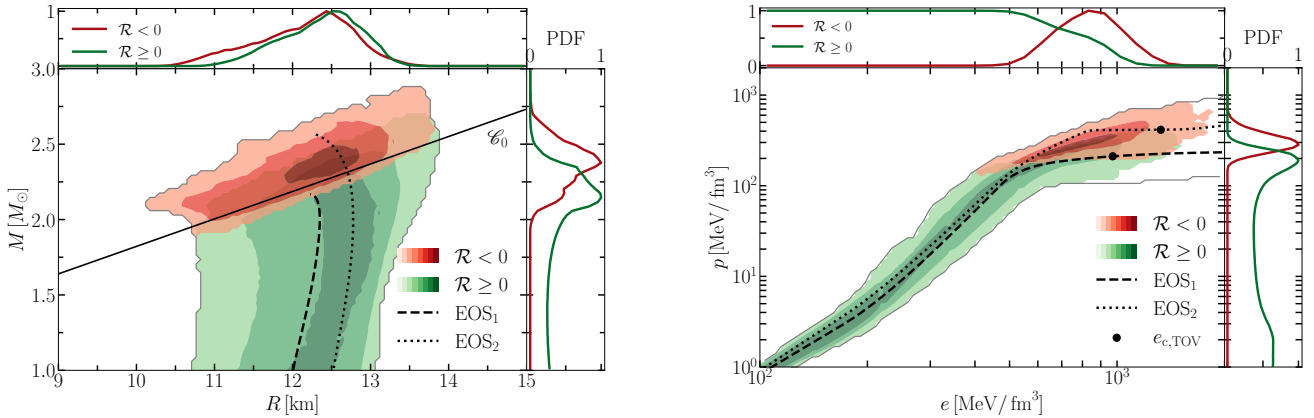


FIG. 2. *Left panel*: Normalised PDFs of the M - R relations for the entire EOS ensemble. The green/red colormap represents the distribution of NSs with non-negative/negative Ricci scalar, everywhere/somewhere inside the star. 1- σ , 2- σ and 100%-confidence intervals are shown from darker to lighter colours. The grey solid line contours the 100%-confidence interval for every stable NS. Shown with a black solid is the “zero-curvature” compactness relation \mathcal{C}_0 , while black dashed and dotted lines mark two reference EOSs ($\text{EOS}_{1,2}$). The top and right parts of the panel report the 100%-confidence intervals of both distributions in the relevant direction. *Right panel*: the same as in the left but for the p - e relations. Marked with black filled circles are the largest energy densities for stable NSs with $\text{EOS}_{1,2}$.

136 piecewise polytropic EOSs that this compactness is quasi-universal, i.e., does not depend significantly on the EOS and is given by $\mathcal{C}_0 = 0.262^{+0.011}_{-0.017}$ [51].

We have found that this result is very robust and indeed our estimate obtained on the basis of the 10^4 EOSs of our sample differs only by 3% and is given by $\mathcal{C}_0 = 0.26911 \pm 0.00004$. We report this “zero-curvature” compactness as a black solid line in the left panel of Fig. 2. The right panel of Fig. 2 provides information that is similar and complementary to that reported in the left panel. More specifically, using the same notation, the panel reports the PDFs of the Ricci scalar as a function of the pressure and energy density of the various EOSs. It is therefore not surprising that the stiffer EOSs tend to lead to NSs with $\mathcal{R} < 0$. Less obvious, however, is the fact that at the highest densities and pressures, all stellar models have negative Ricci scalar in their interior. Overall, the results in Fig. 2 clearly show that the most compact and most massive stars must have $\mathcal{R} < 0$. As we discuss further below, this has direct implications on the the trace anomaly.

B. Gravitational and Baryonic Mass

Measured gravitational wave (GW) signals and light curves from black hole-NS or NS-NS mergers can shed light on the binary properties [see, e.g., 52–54, for some reviews]. The gravitational mass of a NS, M , is the value obtained by integrating Eq. (3) from the center of the star to its surface:

$$M := \int_0^R \frac{dm}{dr} dr, \quad (26)$$

while the baryonic mass of a NS, M_b , is the value obtained by integrating from the center to the surface the following quantity:

$$M_b := 4\pi m_u \int_0^R \frac{n_b r^2 dr}{\sqrt{1 - 2m(r)/r}}, \quad (27)$$

where $m_u \approx 8.3486 \times 10^{-58} M_\odot$ is the atomic mass unit, and n_b is the baryon number density.

Some models to describe the amount of mass and velocity of ejecta are parametrized by the gravitational and baryonic mass of the components, among others [12]. These models allow us to extract information from the binary system by comparing observations with predictions. However, they have degeneracies among these parameters and others, such as spins of the binary and the EOS of NS matter. As a result, (quasi-) universal relations can reduce the dimensionality of the parameter space by trading physical uncertainties against uncertainties in model assumptions. In the left panel of Fig. 3 we show the distribution of gravitational mass M vs. baryonic mass M_b . The solid lines correspond to a quadratic fit of the form

$$M_b = M(1 + a_2 M), \quad (28)$$

as the one presented by Timmes *et al.* [55]. In black we show the fit using a constant $a_2 = 0.075$ from Timmes *et al.* [55], while in green we show the fit with $a_2 = 0.080$ from Gao *et al.* [56]. Using our set of EOSs we find that our best fit gives $a_2 = 0.087$. The absolute value of the residual (using our fit) is $\lesssim 0.08 M_\odot$, corresponding to $\lesssim 3\%$, as shown in the bottom panel. This implies a quasi-universal relation, since given the gravitational mass of a NS, we can now predict its baryonic mass with absolute error $\lesssim 0.08 M_\odot$.

Exploiting the quasi-universal relation (28) it is straightforward to derive another and *linear* quasi-universal relation between the binding energy E_{bin} and the gravitational mass

$$E_{\text{bin}} := M_b - M = a_2 M^2, \quad (29)$$

compare our results with those of [51], we consider the least massive of the two stars.

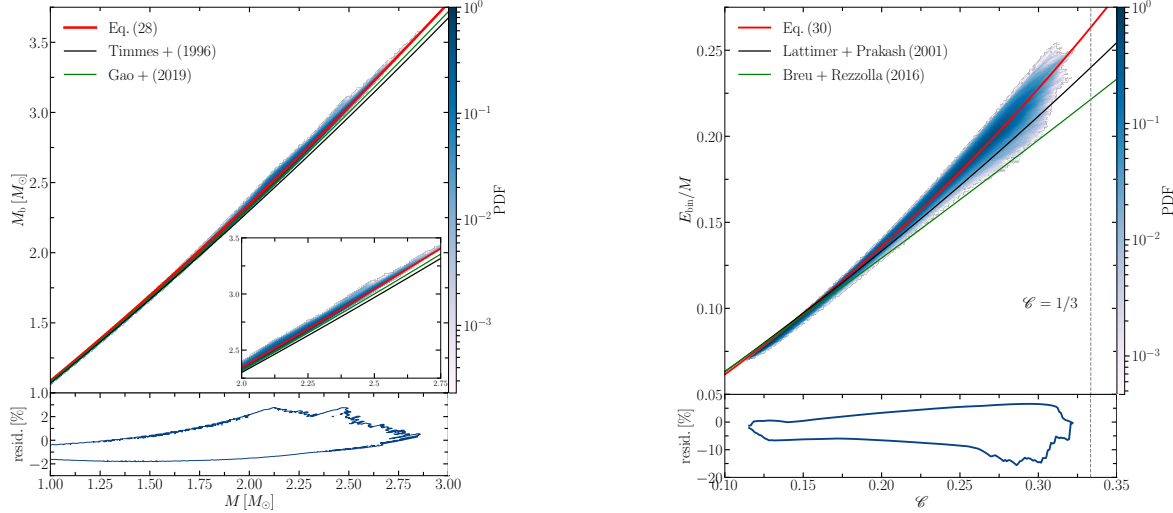


FIG. 3. *Left panel*: distribution of the baryonic mass M_b as a function of gravitational mass M . Shown respectively with red, black and green solid lines are the fits from our work, from Timmes *et al.* [55], and from Gao *et al.* [56]. *Right panel*: distribution of the binding energy E_{bin}/M as a function of the stellar compactness \mathcal{C} . Also in this case, the red line shows our fit to the data, while the black and green lines reports the fit by Lattimer and Prakash [57] and Breu and Rezzolla [58].

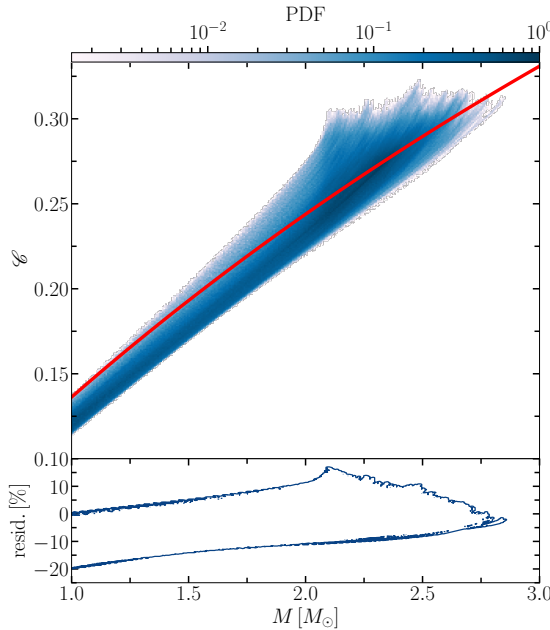


FIG. 4. Distribution of the compactness as a function of the gravitational mass. Shown with a red solid line is the functional behaviour of Eq. (31), which provides a first approximation to the compactness, with an uncertainty of 15-20% for low-mass NSs.

so that a measurement of the gravitational mass of a compact star readily provides a measure of its binding energy. Furthermore, it has long since been known that the normalised binding energy E_{bin}/M is linked via another quasi-universal

relation to the stellar compactness [57, 58]

$$\frac{E_{\text{bin}}}{M} = \frac{c_1 \mathcal{C}}{1 - c_2 \mathcal{C}}, \quad (30)$$

where it is now possible to compute the best-fit values of the coefficients using the extended set of EOSs and find that $c_1 = 0.56270 \pm 0.00005$ and $c_2 = 0.86332 \pm 0.00028$. The result of the fitting is shown with a red line in the right panel of Fig. 3, which reports the distribution of the binding energy E_{bin}/M as a function of the stellar compactness \mathcal{C} . Also in this case, the red line shows our fit to the data, while the black and green lines reports the fit by Lattimer and Prakash [57] and Breu and Rezzolla [58]⁵. Also reported with a vertical black dotted line is the value $\mathcal{C} = 1/3$, which has been recently shown to represent the upper limit of the compactness for NSs satisfying all known physical and astrophysical constraints [50].

As a result, once a measurement of the gravitational mass has been made, the compactness can be estimated as

$$\mathcal{C} = \frac{a_2 M}{c_1 + a_2 c_2 M}. \quad (31)$$

The nonlinear expression (31) is shown with a red solid line in Fig. 4, which reports the distribution of the stellar compactness as a function of the gravitational mass. While the associated uncertainty is not small, it is $\sim 15\text{-}20\%$ for masses $\lesssim 2 M_\odot$ and thus comparable if not smaller than the observational uncertainty [37, 38].

⁵ The reduced χ^2 obtained by Lattimer and Prakash [57] and Breu and Rezzolla [58] for the old dataset was essentially the same. It is only with the new and larger dataset that residuals vary.

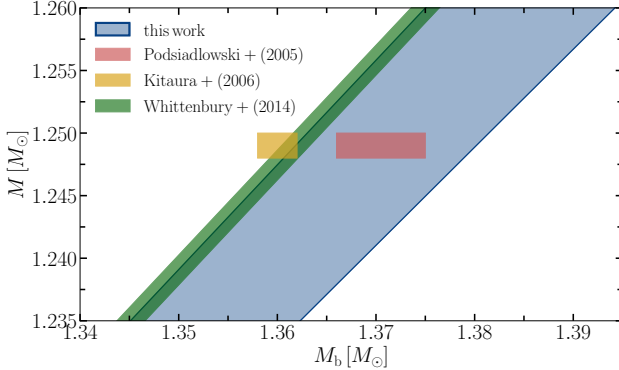


FIG. 5. Different estimates of the baryonic mass for pulsar B in the binary system J0737-3039. Shown with different shadings are the estimates by Podsiadlowski *et al.* [60], i.e., $M_b = 1.366 - 1.375 M_\odot$, by Kitaura *et al.* [61], i.e., $M_b = 1.360 \pm 0.002 M_\odot$ and in this work as taken from the 100%-confidence interval of the distribution in the left panel of Fig. 3 (blue). The predictions by Whittenbury *et al.* [62] are shown as the green stripe.

The importance of the relation (28) between the baryonic and the gravitational mass goes beyond being a tight quasi-universal relation and can actually be employed to obtain an astrophysically relevant result. More specifically, we recall that measurements on the gravitational and baryonic mass of the double pulsar J0737-3039 offer a constraint on the EOS. The gravitational mass of pulsar B in this system is measured to be $1.2489 \pm 0.0007 M_\odot$ [59]. Such low-mass NS may occur for O-Ne-Mg white dwarfs when the core density reaches a critical value, triggering its collapse. Using this hypothesis and assuming that the mass loss after the collapse is at negligible (i.e., up to $10^{-2} M_\odot$), [60] estimated that the corresponding baryonic mass of pulsar B lies between $1.366 M_\odot$ and $1.375 M_\odot$ under the assumption that it was produced in an electron-capture supernova (red-shaded box in Fig. 5). On the other hand, [61] used 1D simulations of type II supernova explosions and estimated a smaller baryonic mass of the resulting NS of $M_b = 1.360 \pm 0.002 M_\odot$ (yellow-shaded box in Fig. 5), due to loss in baryonic mass during the explosion. The 100%-confidence interval for the baryonic mass of pulsar B inferred from our set of EOSs is given by the blue-shaded area between the two horizontal dashed lines indicating the uncertainty in the measurement of the gravitational mass [59]. The two slanted blue solid lines limiting the blue-shaded area are obtained after inverting Eq. (28) and correcting for the spread in the correlation between the two masses. The corresponding analytic expressions are therefore⁶ $M_{l,u} = (\sqrt{1 + 4(b_1)_{l,u} M_b} - 1)/2(b_1)_{l,u} + (b_2)_{l,u}$, where the coefficients are given by $(b_1)_l = 0.1139$, $(b_2)_l = 0.0364$ and $(b_1)_u = 0.0791$, $(b_2)_u = 0.0088$, where "l" and "u" refer to the lower and upper confidence limits, respectively. Finally, the interval obtained by Ref. [62] is shown as the green-shaded stripe, for comparison. Our results show consistency with the

whole baryonic mass range estimated by [60], while the range $M_b = 1.3596 - 1.3620 M_\odot$ is compatible with the estimate of [61].

C. Ricci Curvature and Trace Anomaly

The radial profiles $e = e(r)$ and $p = p(r)$ obtained by solving the TOV equations allow us to compute the relationship between the conformal anomaly $\Delta(r)$ and the Ricci scalar $\mathcal{R}(r)$, via Eq. (22). However, $\mathcal{R}(r)$ and $\Delta(r)$ are simply proportional, hence, the radial dependence of the latter would be as that discussed for the formed in Fig. 1 scaled with the energy density. As a result, it is more interesting to study here the correlation between the two scalar functions. What needs to be borne in mind is that, once an EOS is fixed, for a NS with mass M and radius R , the relation between the trace anomaly and the Ricci scalar will be given by a curve that starts at $(\Delta_s = 1/3, \mathcal{R}_s = 0)$ – the surface of the star (blue asterisk in the left panel of Fig. 6) – and ends at some point $(\Delta_c, \mathcal{R}_c)$ – the centre of the star (coloured filled circles in the left panel of Fig. 6); the grey dashed line is used to mark stars with $M \leq 1.1 M_\odot$, that are astrophysically unlikely. Clearly, the endpoint of such a curve will depend on the value of M and will eventually stop for the largest mass possible for each EOS (red squares in the left panel of Fig. 6). Interestingly, this behaviour not only is non-monotonic, but it can also be double-valued both in the trace anomaly and the Ricci scalar. Furthermore, since we have discussed that Δ and \mathcal{R} generally move towards negative values for the most compact and most massive stars, the behaviour of the normalised Ricci scalar relative to the trace anomaly can be of the type shown in the lower-left panel of Fig. 6, where the curve passes twice through the point $(\Delta = 0, \mathcal{R} = 0)$ for a given "EOS₂". This EOS leads to very massive and compact stars (as can be seen in the left panel of Fig. 2) and hence encounters negative values of the trace anomaly and of the Ricci scalar somewhere inside the corresponding stellar models. This behaviour should be contrasted with that exhibited by a different EOS, i.e., "EOS₁" in the upper-left panel of Fig. 6, which does not produce negative values.

The right panel of Fig. 6, shows with a colormap the PDF of the normalised Ricci scalar as a function of the trace anomaly, at the centre of the stars, for all the EOSs considered in our sample. Clearly, the point $(\Delta_s = 1/3, \mathcal{R}_s = 0)$ is the starting point for all the EOSs and all curves have to pass through it. However, depending on the EOS, the $\mathcal{R} - \Delta$ curve may or may not pass through the point $(\Delta = 0, \mathcal{R} = 0)$, and may end at either $\mathcal{R}_c < 0$, $\mathcal{R}_c = 0$, or $\mathcal{R}_c > 0$. Marked with solid brown lines are the minimum [maximum] normalised Ricci scalar $(\mathcal{R}_c M^2)_{\min} [(\mathcal{R}_c M^2)_{\max}]$ and the minimum trace-anomaly $\Delta_{c,\min}$ found with our set of EOSs.

The global minimum value of the Ricci scalar achieved inside any NS is found to be $\mathcal{R}_{\min} = -2.510 \times 10^{-12} \text{ cm}^{-2}$; while the global maximum value is $\mathcal{R}_{\max} = 2.383 \times 10^{-12} \text{ cm}^{-2}$. The global minimum of the trace anomaly turns out to be $\Delta_{\min} = -0.227$. These three values can be taken as bounds for both the Ricci scalar and the trace anomaly present in the most

⁶ These analytic expressions are accurate in the range $M_b/M_\odot \in [1.3, 2.3]$.

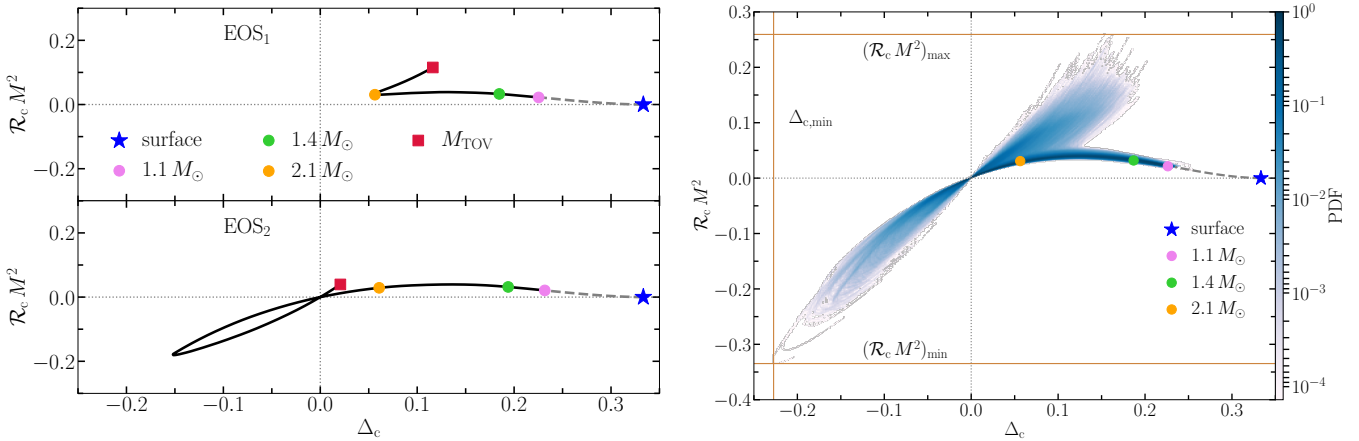


FIG. 6. *Left panel*: relation between the trace anomaly and the Ricci scalar for two representative EOSs: EOS₁ (top part) and EOS₂ (bottom part). For each curve, the relation will be represented by a curve that starts at the surface of the star where $\Delta_s = 1/3$, $\mathcal{R}_s = 0$ (blue asterisk) and ends at the centre of the star where Δ_c , \mathcal{R}_c (coloured filled circles); the grey dashed line is used to mark stars with $M \leq 1.1 M_\odot$, that are astrophysically unlikely, while the red squares mark the largest possible mass. Depending on the EOS, the black curve may not reach $\Delta_c = 0$ (as for the case of EOS₁), or reach it and perform a loop in the negative $(\mathcal{R}_c, \Delta_c)$ region (as for the case of EOS₂). *Right panel*: the same as in the left but shown for all the EOSs considered in terms of a normalised PDF. Also shown with vertical and horizontal brown lines are, respectively: the minimum value of central conformal anomaly $\Delta_{c,\min}$, and the minimum (maximum) value of normalized central value of Ricci scalar $(\mathcal{R}_c M^2)_{\min}$ ($(\mathcal{R}_c M^2)_{\max}$).

compact objects composed of regular matter in the Universe.

We conclude this Section by commenting on the result that the Ricci scalar can achieve negative values in the interior of massive stars. First, we note that a negative value of the Ricci scalar does not reflect a violation of any of the energy conditions [31]. Indeed, since the energy density and pressure are always positive in all of our EOSs, the weak (i.e., $e + p \geq 0$, $e \geq 0$) and strong (i.e., $e + p \geq 0$, $e + 3p \geq 0$) energy conditions are satisfied for all of them. In addition, the dominant energy condition (i.e., $e \geq |p|$), can be recast into a condition on the trace anomaly, i.e., $\Delta > -2/3$, which is clearly satisfied by all of the EOSs (see right panel of Fig. 6). Second negative values of the Ricci scalar may appear somewhat surprising because intuition suggests that curvature should always be positive in the star and actually decrease almost monotonically⁷ from the centre. This intuition is indeed correct but does not apply to the Ricci scalar but, rather, to the Kretschmann scalar.

Figure 7 provides an analogue to the rightmost panel of Fig. 1 but for the dimensionless Kretschmann scalar, i.e., $\mathcal{K}_1 M^4$, and for stellar models with $M = M_{\text{TOV}}$. Note that in this case $\mathcal{K}_1 M^4$ is always positive and decreasing outwards, highlighting that the Ricci scalar is simply not a very representative indicator of the curvature in a star as it is not in a Schwarzschild (Kerr) black hole, since it is zero everywhere apart from the singularity where it is ill-defined. The Kretschmann scalar, on the other hand, not only respects the expected behaviour (which is similar to that in a black hole) but it is also larger for more compact and massive stars. This is illustrated in the inset of Fig. 7 which reports with a green (red)

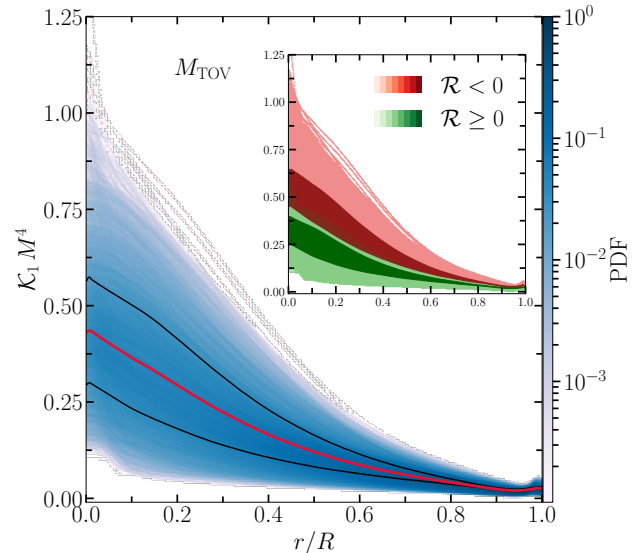


FIG. 7. Normalized PDFs of the radial profiles of the normalized Kretschmann scalar $\mathcal{K}_1 M^4$ for maximum-mass stars. Also in this case, the red lines mark the median values of the distribution, while black lines correspond to $1-\sigma$ confidence limits. Shown instead in the inset are the same distributions as in the main panel but with red (green) colormaps to mark the regions where the NSs have $\mathcal{R} < 0$ ($\mathcal{R} \geq 0$) somewhere in their interior. Darker/lighter shadings refer to $1-\sigma$ and 100% confidence levels, respectively.

⁷ The strict monotonicity is broken at the stellar surface because of the contributions coming from I_1 ; see also [25].

colourmap the Kretschmann scalar for stellar models where $\mathcal{R} > 0$ everywhere ($\mathcal{R} \leq 0$ somewhere) inside the star, and where the dark and light shadings cover the $1-\sigma$ and 100% -confidence intervals, respectively. Finally, we note that the value of $\mathcal{K}_1 M_{\text{TOV}}^4$ at the centre of the star is directly correlated

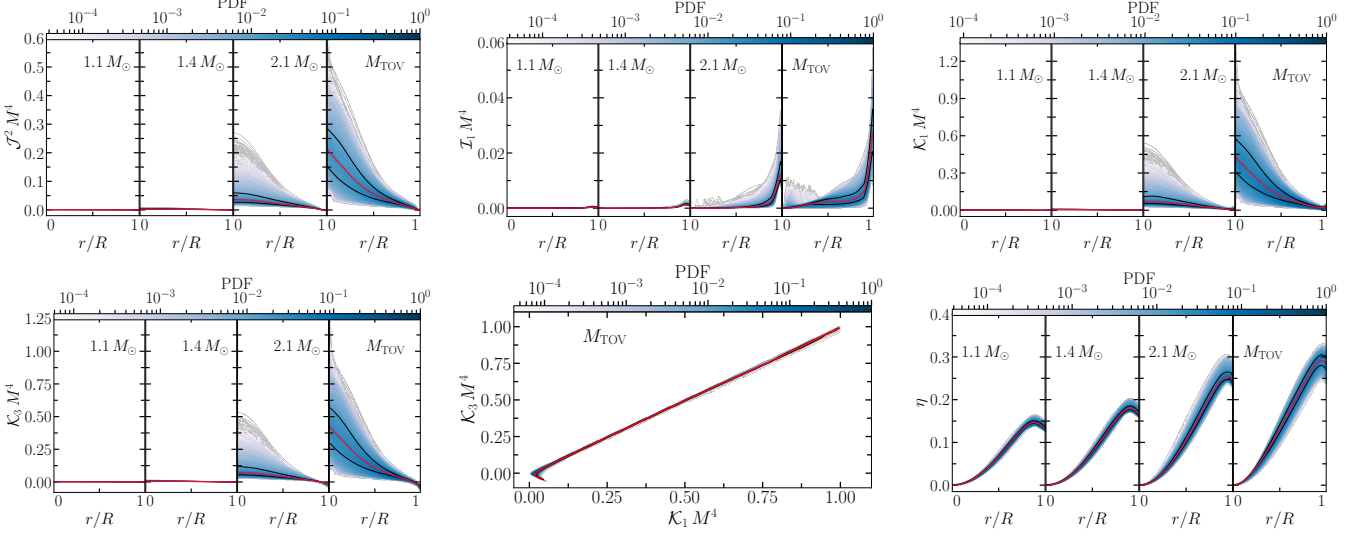


FIG. 8. Normalized PDFs of the radial profiles of various normalised curvature scalars. From top left, we report \mathcal{J}^2 , I_1 , \mathcal{K}_1 , and \mathcal{K}_3 properly rescaled by a factor M^4 to make them dimensionless, and for the same reference masses of $M = 1.1, 1.4, 2.1 M_\odot$, and M_{TOV} . The fifth panel from the top left highlights the close correlations between \mathcal{K}_3 and \mathcal{K}_1 , while the last panel shows the radial profile of the compactness function, $\eta(r) := m(r)/r$. Also here, the red lines mark the median values of the distribution, while black lines correspond to $1-\sigma$ confidence limits.

with the corresponding value of $\mathcal{R} M_{\text{TOV}}^2$, i.e., is larger for those stellar models which have the smallest and negative values of $\mathcal{R} M_{\text{TOV}}^2$. This behaviour is not obvious to expect from Eq. (15), which relates \mathcal{K}_1 to \mathcal{R} and \mathcal{J}^2 ($I_1 = 0$ at the centre of the star; see Fig. 8). Yet, as the stellar centre is approached, $2\mathcal{J}^2$ grows more rapidly than $\mathcal{R}^2/3$, hence ensuring that \mathcal{K}_1 not only is positive, but it is also larger for more massive stars.

D. Other Curvature invariants

Figure 8 provides information that is complementary to that in Fig. 1, namely, it reports the radial profiles of the other curvature scalars described in Section I. Starting from the top left, we report the PDFs for \mathcal{J}^2 , I_1 , \mathcal{K}_1 , and \mathcal{K}_3 properly rescaled by a factor M^4 to make them dimensionless, and for the same reference masses of $M = 1.1, 1.4, 2.1 M_\odot$, and M_{TOV} .

As expected from Eq. (23), the full contraction of the Ricci tensor, \mathcal{J}^2 , decreases from the centre to the stellar surface and because \mathcal{J}^2 is proportional to the squared energy density e^2 . In this respect, this scalar is similar to the Ricci scalar \mathcal{R} , since it is related to the part of the gravitational field that is tied directly and locally to the matter sources of the field. On the other hand, the full contraction of the Weyl tensor, I_1 , depends on the squared difference between the mean energy density and the energy density, $(\bar{e} - e)^2$. While close to the centre of the NS, $\bar{e} \sim e$ and $I_1 \sim 0$, with increasing radial coordinate, the inequality $\bar{e} > e$ becomes steeper. As a result, at lower densities and close to the surface, the relevant quantity for I_1 is $\bar{e} = 3m/(4\pi r^3)$, so that I_1 increases until it reaches a maximum near the surface and then decreases. This decreasing behaviour is due to the fact that the integrated mass increases at a slower rate than $\propto r^3$ as it approaches the surface. Because outside the NS it will decrease as $\propto M^2/r^6$ (not shown in

Fig. 8), we can interpret the scalar I_1 as the curvature produced by the gravitational field of the mass distribution $m(r)$ or, alternatively, as the deviation of the local curvature at a given radial position and from the average one up to that position.

On the other hand, when considering the radial profiles of the Kretschmann scalar, \mathcal{K}_1 , the PDFs show the behaviour dictated by Eq. (15), so that at the core of the NSs, this scalar is mainly determined by $2\mathcal{J}^2$, and close to the surface it approaches I_1 ; in the vacuum outside the NSs (not shown in Fig. 6), $\mathcal{K}_1 = I_1$. Thus, \mathcal{K}_1 can be thought to be associated with both the local energy distribution $e(r)$ and with the mass distribution $m(r)$, much as in a Newtonian gravitational potential.

Finally, when exploring the radial behaviour of the Euler scalar \mathcal{K}_3 , it is remarkable to note the similarities, both qualitative and quantitative, with the Kretschmann scalar \mathcal{K}_1 . This is in the middle panel of the second row in Fig. 8, which reports the PDF of \mathcal{K}_3 as a function of \mathcal{K}_1 . It is then apparent that using Eqs. (15) and (17) and with the exception of the stellar surfaces – where $\mathcal{K}_1 \simeq 0$ – we infer

$$\mathcal{K}_3 \sim \mathcal{K}_1 \sim 2\mathcal{J}^2, \quad (32)$$

$$2\mathcal{J}^2 \gg I_1 - \mathcal{R}/3, \quad (33)$$

$$2\mathcal{J}^2 \gg -I_1 - 2\mathcal{R}/3. \quad (34)$$

Near the stellar surfaces, on the other hand, the term $-I_1$ dominates, so that at the lowest densities $\mathcal{K}_3 \approx -\mathcal{K}_1 \lesssim 0$. The fact that the Euler scalar can reach negative values near the stellar surface makes it less useful than the Kretschmann scalar, even though it is very similar to the former for most of the stellar structure. Finally, reported in the bottom-right panel of Fig. 8, is the radial profile of the compactness function, $\eta(r) := m(r)/r$, which exhibits an increasing behaviour in the stellar core, until a local maximum is produced by a growth

in the mass function that is slower than $\propto r$, thus producing a decrease of η as it approaches the stellar surface; this behaviour was already remarked by Eksi *et al.* [25].

IV. CONCLUSION

Motivated by the lack of information about how the curvature varies inside NSs and how it depends on different EOSs, we have performed the first systematic analysis of curvature invariants in these compact objects. To this end, we have employed the approach presented by Altiparmak *et al.* [18] and constructed a set of 10^4 EOSs parameterized in term of the sound speed and that satisfy the constraints from nuclear theory and perturbative QCD, as well as measurements of NS masses, radii, and gravitational waves from binary NS mergers.

In this way, and considering the principal curvature invariants of the Riemann tensor (e.g., the Kretschmann, Chern-Pontryagin, Euler invariants), it was possible to show that NSs can have a negative value of the Ricci scalar \mathcal{R} somewhere in their interior. Indeed, this property is so common that about $\sim 50\%$ of our EOSs produce one or more stars with negative Ricci curvature inside the star. The negative curvature is found mostly but not exclusively at the highest densities and pressures, and predominantly for stiff EOSs and for the most compact and most massive stars. Furthermore, we can calculate a statistically improved estimate of the “zero-curvature” compactness relation, finding that the value of the compactness $\mathcal{C} := M/R$ at which the stellar model has zero Ricci curvature at the center, finding it differs by only $\sim 3\%$ from previous estimates obtained with a much smaller set of EOSs [51].

A negative Ricci scalar may appear counter-intuitive as one may be induced to think that curvature should always be positive in the star and actually decrease almost monotonically from the centre. In practice, this result simply highlights that the Ricci scalar is not a very representative indicator of the curvature in a star, just as it is not in a Schwarzschild or a Kerr spacetime. Instead, a much better indicator of the curvature is the Kretschmann scalar \mathcal{K}_1 (and its related Euler scalar \mathcal{K}_3) as it possesses all the expected properties of positivity and monotonicity.

Our analysis of the general gravitational properties of NSs has also considered the well-known quasi-universal relation between the stellar gravitational mass M and the baryonic mass M_b , and we have derived a new and improved analytic fit of the data that reproduces it very closely, with a maxi-

mum variance of only $\sim 3\%$ across the whole set of EOSs. As a practical application, we use the new quasi-universal expression to obtain a new estimate of the baryonic mass of the double pulsar J0737-3039.

Finally, using the relation between the Ricci scalar and the trace anomaly Δ , we determine under which conditions Δ vanishes or becomes negative in NSs, and also set general upper and lower bounds on the values of the Ricci scalar at the stellar centre and, more importantly, the largest violation (i.e., the largest negative value) of the trace anomaly in the interior of a NS. While our results have been confined to nonrotating stars, very little is presently known about the curvature behaviour in compact rotating stars, especially when their spin is near the maximal one. We plan to investigate these aspects in future work.

ACKNOWLEDGEMENTS

We thank Dany Page, Sergio Mendoza, Yavuz Eksi for insightful discussions, and Mabel Osorio-Archila for useful discussions and careful reading of the original manuscript. Partial funding comes from the ERC Advanced Grant “JETSET: Launching, propagation and emission of relativistic jets from binary mergers and across mass scales” (Grant No. 884631). I. G. acknowledges that this work was made possible with the support of a scholarship from the German Academic Exchange Service (DAAD), through the Research Grants - Doctoral Programmes in Germany, personal reference number 91940015. C. E. acknowledges support by the Deutsche Forschungsgemeinschaft (DFG, German Research Foundation) through the CRC-TR 211 “Strong-interaction matter under extreme conditions” – project number 315477589 – TRR 211. L. R. acknowledges the Walter Greiner Gesellschaft zur Förderung der physikalischen Grundlagenforschung e.V. through the Carl W. Fueck Laureatus Chair. The calculations were performed in part on Universidad Nacional Autónoma de México’s server Geminga and on the ITP Supercomputing Cluster Calea.

DATA AVAILABILITY

Data is available upon reasonable request from the corresponding author.

[1] E. S. Fraga, A. Kurkela, and A. Vuorinen, *Astrophys. J. Lett.* **781**, L25 (2014), arXiv:1311.5154 [nucl-th].

[2] E. R. Most, L. R. Weih, L. Rezzolla, and J. Schaffner-Bielich, *Phys. Rev. Lett.* **120**, 261103 (2018), arXiv:1803.00549 [gr-qc].

[3] E. Annala, T. Gorda, A. Kurkela, J. Nättälä, and A. Vuorinen, *Nature Physics* **16**, 907 (2020).

[4] M. Ferreira, R. C. Pereira, and C. Providência, *Phys. Rev. D* **103**, 123020 (2021).

[5] O. Komoltsev and A. Kurkela, *Phys. Rev. Lett.* **128**, 202701 (2022), arXiv:2111.05350 [nucl-th].

[6] E. Annala, T. Gorda, E. Katerini, A. Kurkela, J. Nättälä, V. Paschalidis, and A. Vuorinen, *Physical Review X* **12**, 011058 (2022), arXiv:2105.05132 [astro-ph.HE].

[7] R. Somasundaram, I. Tews, and J. Margueron, *arXiv e-prints*, arXiv:2204.14039 (2022), arXiv:2204.14039 [nucl-th].

[8] T. Gorda, O. Komoltsev, and A. Kurkela, *The Astrophysical Journal* **950**, 107 (2023).

[9] Y. Fujimoto, K. Fukushima, K. Hotokezaka, and K. Kyutoku, Phys. Rev. Lett. **130**, 091404 (2023).

[10] M. Albino, T. Malik, M. Ferreira, and C. Providência, Phys. Rev. D **110**, 083037 (2024).

[11] K. Fukushima, Journal of Subatomic Particles and Cosmology , 100066 (2025).

[12] M. Coughlin, T. Dietrich, K. Kawaguchi, S. Smartt, C. Stubbs, and M. Ujevic, Astrophys. J. **849**, 12 (2017), arXiv:1708.07714 [astro-ph.HE].

[13] C. C. Moustakidis, T. Gaitanos, C. Margaritis, and G. A. Lalazissis, Physical Review C **95**, 045801 (2017), arXiv:1608.00344 [nucl-th].

[14] I. Tews, J. Carlson, S. Gandolfi, and S. Reddy, Astrophys. J. **860**, 149 (2018), arXiv:1801.01923 [nucl-th].

[15] C. Margaritis, P. S. Koliogiannis, and C. C. Moustakidis, Phys. Rev. D **101**, 043023 (2020), arXiv:1910.05767 [nucl-th].

[16] A. Kanakis-Pegios, P. S. Koliogiannis, and C. C. Moustakidis, Symmetry **13**, 183 (2021), arXiv:2012.09580 [astro-ph.HE].

[17] M. Hippert, E. S. Fraga, and J. Noronha, Phys. Rev. D **104**, 034011 (2021), arXiv:2105.04535 [nucl-th].

[18] S. Altiparmak, C. Ecker, and L. Rezzolla, Astrophys. J. Lett. **939**, L34 (2022), arXiv:2203.14974 [astro-ph.HE].

[19] Y. Fujimoto, K. Fukushima, L. D. McLerran, and M. Praszalowicz, Phys. Rev. Lett. **129**, 252702 (2022), arXiv:2207.06753 [nucl-th].

[20] M. Marczenko, L. McLerran, K. Redlich, and C. Sasaki, Phys. Rev. C **107**, 025802 (2023), arXiv:2207.13059 [nucl-th].

[21] C. Ecker and L. Rezzolla, Mon. Not. R. Astron. Soc. **519**, 2615 (2023), arXiv:2209.08101 [astro-ph.HE].

[22] E. Annala, T. Gorda, J. Hirvonen, O. Komoltsev, A. Kurkela, J. Nättälä, and A. Vuorinen, Nature Communications **14** (2023), 10.1038/s41467-023-44051-y.

[23] M. Marczenko, J. Subatomic Part. Cosmol. **3**, 100043 (2025), arXiv:2502.10847 [nucl-th].

[24] C. Ecker, N. Jokela, and M. Järvinen, arXiv e-prints , arXiv:2506.10065 (2025), arXiv:2506.10065 [astro-ph.HE].

[25] K. Y. Ekş, C. Güngör, and M. M. Türkoğlu, Physical Review D **89** (2014), 10.1103/physrevd.89.063003.

[26] X.-T. He, F. J. Fattoyev, B.-A. Li, and W. G. Newton, Phys. Rev. C **91**, 015810 (2015).

[27] H. C. Das, A. Kumar, B. Kumar, S. K. Biswal, and S. K. Patra, Journal of Cosmology and Astroparticle Physics **2021**, 007 (2021), arXiv:2007.05382 [nucl-th].

[28] S. K. Biswal, H. C. Das, A. Kumar, B. Kumar, R. Jena, P. Dash, and S. K. Patra, International Journal of Modern Physics E **34**, 2550009 (2025), arXiv:2012.13673 [astro-ph.HE].

[29] S. Ghosh, B. Kumar, and S. Mahapatra, arXiv preprint arXiv:2508.08866 (2025).

[30] A. C. Khunt, K. Y. Ekş, and P. C. Vinodkumar, arXiv e-prints , arXiv:2512.24194 (2025), arXiv:2512.24194 [gr-qc].

[31] L. Rezzolla and O. Zanotti, *Relativistic Hydrodynamics* (Oxford University Press, 2013).

[32] G. Baym, C. Pethick, and P. Sutherland, Astrophys. J. **170**, 299 (1971).

[33] K. Hebeler, J. M. Lattimer, C. J. Pethick, and A. Schwenk, Astrophys. J. **773**, 11 (2013), arXiv:1303.4662 [astro-ph.SR].

[34] J. Antoniadis, P. C. C. Freire, N. Wex, T. M. Tauris, R. S. Lynch, and et al., Science **340**, 448 (2013), arXiv:1304.6875 [astro-ph.HE].

[35] H. T. Cromartie, E. Fonseca, S. M. Ransom, P. B. Demorest, Z. Arzoumanian, H. Blumer, P. R. Brook, M. E. DeCesar, T. Dolch, J. A. Ellis, R. D. Ferdman, E. C. Ferrara, N. Garver-Daniels, P. A. Gentile, M. L. Jones, M. T. Lam, D. R. Lorimer, R. S. Lynch, M. A. McLaughlin, C. Ng, D. J. Nice, T. T. Penucci, R. Spiewak, I. H. Stairs, K. Stovall, J. K. Swiggum, and W. W. Zhu, Nature Astronomy **4**, 72 (2020), arXiv:1904.06759 [astro-ph.HE].

[36] E. Fonseca, H. T. Cromartie, T. T. Pennucci, P. S. Ray, A. Y. Kirichenko, S. M. Ransom, P. B. Demorest, I. H. Stairs, Z. Arzoumanian, L. Guillemot, A. Parthasarathy, M. Kerr, I. Cognard, P. T. Baker, H. Blumer, P. R. Brook, M. DeCesar, T. Dolch, F. A. Dong, E. C. Ferrara, W. Fiore, N. Garver-Daniels, D. C. Good, R. Jennings, M. L. Jones, V. M. Kaspi, M. T. Lam, D. R. Lorimer, J. Luo, A. McEwen, J. W. McKee, M. A. McLaughlin, N. McMann, B. W. Meyers, A. Naidu, C. Ng, D. J. Nice, N. Pol, H. A. Radovan, B. Shapiro-Albert, C. M. Tan, S. P. Tendulkar, J. K. Swiggum, H. M. Wahl, and W. W. Zhu, Astrophys. J. Lett. **915**, L12 (2021), arXiv:2104.00880 [astro-ph.HE].

[37] M. C. Miller, F. K. Lamb, A. J. Dittmann, S. Bogdanov, Z. Arzoumanian, K. C. Gendreau, S. Guillot, W. C. G. Ho, J. M. Lattimer, M. Loewenstein, S. M. Morsink, P. S. Ray, M. T. Wolff, C. L. Baker, T. Cazeau, S. Manthripragada, C. B. Markwardt, T. Okajima, S. Pollard, I. Cognard, H. T. Cromartie, E. Fonseca, L. Guillemot, M. Kerr, A. Parthasarathy, T. T. Pennucci, S. Ransom, and I. Stairs, Astrophys. J. Lett. **918**, L28 (2021), arXiv:2105.06979 [astro-ph.HE].

[38] T. E. Riley, A. L. Watts, P. S. Ray, S. Bogdanov, S. Guillot, S. M. Morsink, A. V. Bilous, Z. Arzoumanian, D. Choudhury, J. S. Deneva, K. C. Gendreau, A. K. Harding, W. C. G. Ho, J. M. Lattimer, M. Loewenstein, R. M. Ludlam, C. B. Markwardt, T. Okajima, C. Prescod-Weinstein, R. A. Remillard, M. T. Wolff, E. Fonseca, H. T. Cromartie, M. Kerr, T. T. Pennucci, A. Parthasarathy, S. Ransom, I. Stairs, L. Guillemot, and I. Cognard, Astrophys. J. Lett. **918**, L27 (2021), arXiv:2105.06980 [astro-ph.HE].

[39] T. E. Riley, A. L. Watts, S. Bogdanov, P. S. Ray, R. M. Ludlam, S. Guillot, Z. Arzoumanian, C. L. Baker, A. V. Bilous, D. Chakrabarty, K. C. Gendreau, A. K. Harding, W. C. G. Ho, J. M. Lattimer, S. M. Morsink, and T. E. Strohmayer, Astrophys. J. Lett. **887**, L21 (2019), arXiv:1912.05702 [astro-ph.HE].

[40] M. C. Miller, F. K. Lamb, A. J. Dittmann, S. Bogdanov, Z. Arzoumanian, K. C. Gendreau, S. Guillot, A. K. Harding, W. C. G. Ho, J. M. Lattimer, R. M. Ludlam, S. Mahmoodifar, S. M. Morsink, P. S. Ray, T. E. Strohmayer, K. S. Wood, T. Enoto, R. Foster, T. Okajima, G. Prigozhin, and Y. Soong, Astrophys. J. Lett. **887**, L24 (2019), arXiv:1912.05705 [astro-ph.HE].

[41] The LIGO Scientific Collaboration, the Virgo Collaboration, B. P. Abbott, R. Abbott, T. D. Abbott, F. Acernese, K. Ackley, C. Adams, T. Adams, P. Addesso, R. X. Adhikari, V. B. Adya, and et al. (LIGO Scientific Collaboration and Virgo Collaboration), Physical Review X **9**, 011001 (2019), arXiv:1805.11579 [gr-qc].

[42] J. Goodman and J. Weare, Communications in applied mathematics and computational science **5**, 65 (2010).

[43] J. Géhéniau and R. Debever, Bulletins de l'Académie Royale de Belgique **42**, 114 (1956).

[44] C. Ecker, K. Topolski, M. Järvinen, and A. Stehr, Phys. Rev. D **111**, 023001 (2025), arXiv:2402.11013 [astro-ph.HE].

[45] T. Demircik, C. Ecker, and M. Järvinen, Phys. Rev. X **12**, 041012 (2022), arXiv:2112.12157 [hep-ph].

[46] C. Cherubini, D. Bini, S. Capozziello, and R. Ruffini, Int. J. Mod. Phys. D **11**, 827 (2002), arXiv:gr-qc/0302095.

[47] J. Plebanski and J. Stachel, Journal of Mathematical Physics **9**, 269 (1968).

[48] Y. B. Zel'dovich, Zh. Eksp. Teor. Fiz. **41**, 1609 (1961).

[49] S. Blomqvist, C. Ecker, T. Gorda, and A. Vuorinen, arXiv e-prints , arXiv:2512.19477 (2025), arXiv:2512.19477 [astro-ph.HE].

- [50] L. Rezzolla and C. Ecker, arXiv e-prints , arXiv:2510.12870 (2025), arXiv:2510.12870 [gr-qc].
- [51] D. M. Podkowka, R. F. P. Mendes, and E. Poisson, Phys. Rev. D **98**, 064057 (2018), arXiv:1807.01565 [gr-qc].
- [52] L. Baiotti and L. Rezzolla, Rept. Prog. Phys. **80**, 096901 (2017), arXiv:1607.03540 [gr-qc].
- [53] V. Paschalidis, Classical and Quantum Gravity **34**, 084002 (2017), arXiv:1611.01519 [astro-ph.HE].
- [54] D. Radice, S. Bernuzzi, and A. Perego, Annual Review of Nuclear and Particle Science **70**, 95 (2020), arXiv:2002.03863 [astro-ph.HE].
- [55] F. X. Timmes, S. E. Woosley, and T. A. Weaver, Astrophys. J. **457**, 834 (1996), astro-ph/9510136.
- [56] H. Gao, S.-K. Ai, Z.-J. Cao, B. Zhang, Z.-Y. Zhu, A. Li, N.-B. Zhang, and A. Bauswein, Frontiers of Physics **15**, 24603 (2020), arXiv:1905.03784 [astro-ph.HE].
- [57] J. M. Lattimer and M. Prakash, Astrophys. J. **550**, 426 (2001), arXiv:astro-ph/0002232 [astro-ph].
- [58] C. Breu and L. Rezzolla, Mon. Not. R. Astron. Soc. **459**, 646 (2016), arXiv:1601.06083 [gr-qc].
- [59] M. Kramer, I. H. Stairs, R. N. Manchester, M. A. McLaughlin, A. G. Lyne, R. D. Ferdman, M. Burgay, D. R. Lorimer, A. Possenti, N. D'Amico, J. M. Sarkissian, G. B. Hobbs, J. E. Reynolds, P. C. C. Freire, and F. Camilo, Science **314**, 97 (2006), astro-ph/0609417.
- [60] P. Podsiadlowski, J. D. M. Dewi, P. Lesaffre, J. C. Miller, W. G. Newton, and J. R. Stone, Monthly Notices of the Royal Astronomical Society **361**, 1243–1249 (2005).
- [61] F. S. Kitaura, H. Janka, and W. Hillebrandt, Astron. Astrophys. **450**, 345 (2006), arXiv:astro-ph/0512065.
- [62] D. L. Whittenbury, J. D. Carroll, A. W. Thomas, K. Tsushima, and J. R. Stone, Physical Review C **89** (2014), 10.1103/physrevc.89.065801.